Journal of Alloys and Compounds 992 (2024) 174545

Contents lists available at ScienceDirect

Journal of Alloys and Compounds

journal homepage: www.elsevier.com/locate/jalcom

Spectroscopic and theoretical investigation of Brønsted acid sites in amorphous mixed Zr-Si oxide nanoparticles

Nicola Scotti [a,1], Silvia Borsacchi [b,c,1], Susanna Monti [b], Anna Zimina [d], Claudio Evangelisti [b], Marco Geppi [c,e], Paolo Dambruoso [f], Giovanni Barcaro [g,*], Filippo Bossola [a,*], Vladimiro Dal Santo [a], Nicoletta Ravasio [a]

[a] Istituto di Scienze e Tecnologie Chimiche "Giulio Natta" – Consiglio Nazionale delle Ricerche (CNR-SCITEC), Via C. Golgi 19, Milano 20133, Italy
[b] Istituto di Chimica dei Composti OrganoMetallici – Consiglio Nazionale delle Ricerche (CNR-ICCOM), Via G. Moruzzi 1, Pisa 56124, Italy
[c] Center for Instrument Sharing of the University of Pisa (CISUP), Pisa 56126, Italy
[d] Institute of Catalysis Research and Technology (IKFT), Karlsruhe Institute of Technology, Eggenstein-Leopoldshafen76344, Germany
[e] Dipartimento di Chimica e Chimica Industriale – Università di Pisa, Via G. Moruzzi 13, Pisa 56124, Italy
[f] Istituto per la Sintesi Organica e la Fotoreattività – Consiglio Nazionale delle Ricerche (CNR-ISOF), Via P. Gobetti 101, Bologna 40129, Italy
[g] Istituto per i Processi Chimico-Fisici – Consiglio Nazionale delle Ricerche (CNR-IPCF), Via G. Moruzzi 1, Pisa 56124, Italy

ARTICLE INFO

Keywords:
Zr-Si mixed oxides
Brønsted acid sites
Multiscale modeling
29Si MAS NMR
XAS

ABSTRACT

Mixed Zr-Si oxide nanoparticles were investigated to disclose the relation between the Brønsted acidity of these materials and the atomic composition of the particles. To this aim, we combined experimental structural characterizations via X-ray absorption and Solid State Nuclear Magnetic Resonance spectroscopies with Reactive Molecular Dynamics simulations and Quantum Chemistry calculations. Despite the materials' complexity, we identified the surface hydrogens responsible for the Brønsted acidity by estimating the adsorption energy of pyridine on several topologically distinct hydroxyl groups. Among the investigated sites, the hydrogens connected to the oxygen atoms bridging surface Zr and Si atoms (i.e., Zr-O(H)-Si) exhibited the most marked Brønsted acidity. The agreement of all the employed techniques demonstrates how the proposed concerted characterization effectively elucidates these complex amorphous materials' structure/properties relationships. These new insights allowed us to develop a material with exceptionally high Brønsted acid character that outperformed benchmark silica-alumina and sulfonated zirconia in the dehydrogenation reaction of 1-octanol to produce olefins.

1. Introduction

Mixed oxides have puzzled researchers for a long time since they often display properties that are not a linear combination of those of the single components [1–6]. Among many, the formation of Brønsted acid sites (BAS) is arguably the most intriguing feature because of their importance in heterogeneous catalysis, both for traditional processes and, in the last years, in the fast-growing field of the sustainable chemistry and biomass upgrading [7,8]. Apart from the most notorious cases, such as zeolites, ZrO_2-based oxides have attracted much attention [1,9–15]. Like zeolites, these materials can display Brønsted acidity when appropriately treated at particular Zr/Si ratios [4,5,16–19]. Unlike zeolites, where the cation exchange mechanism is well-understood, little is known about the BAS nature of Zr mixed oxides despite many years of investigations, which often have come to contradictory conclusions. Several models have been proposed [1,2,3,6,20–23], with the most famous being Tanabe's one [6]. These models attempt to predict the formation of BAS for a relatively wide range of Zr/Si ratios, essentially based on the charge imbalance caused by the different valence of the elements and their relative abundance. In these models, the coordination numbers are typically considered constant [2,6], and ideal electronegativity values are assumed [21]; also, the crystallinity of real samples is often neglected. For instance, Tanabe's model cannot predict the Brønsted acidity found in amorphous Zr-Si mixed oxides at Zr/Si atomic ratios of 1 [4] [16]. Nevertheless the location of the BAS sites has been postulated a few times based on experimental and theoretical

* Corresponding authors.
E-mail addresses: giovanni.barcaro@cnr.it (G. Barcaro), filippo.bossola@scitec.cnr.it (F. Bossola).
[1] Equally contributing authors.

https://doi.org/10.1016/j.jallcom.2024.174545
Received 8 February 2024; Received in revised form 16 April 2024; Accepted 18 April 2024
Available online 24 April 2024

approaches, finding silanol groups close to Zr centers (Zr-O-Si(OH)) [17], generic hydroxyl groups on electron-poor Zr centers ($Zr(OH)_x$) [16] or, like in the case of zeolites, bridging hydroxyl groups (Zr-O(H)-Si) [12,18,24,25]. However, there are a few points on which there is consensus. First, BAS can be found in both crystalline [5,12,17] and amorphous [4,5,18,25,26] materials, which indicates that the crystallinity does not influence their formation. Second, a correlation between BAS and the number of Zr-O-Si heterolinks has been consistently observed [5,16,17,25,26].

Identifying such BAS will provide precious insights into the factors driving their formation and may be exploited to manufacture catalytic materials with highly controlled acid-base profiles. Harsh treatments with mineral acids will no longer be required to introduce BAS, thus preserving the typical multifunctional nature of ZrO_2-based catalysts. Undesired superacidity may also be avoided, or at least modulated, so that the deposition of carbonaceous materials can be limited during catalytic transformations [27].

In this work we provide further evidence for identifying Brønsted acid sites in Zr-Si mixed-oxides. For this purpose, we adopted a highly intertwined experimental and theoretical approach to disclose the morphology of the synthesized materials and then to pinpoint the BAS through a combination of X-ray Absorption Spectroscopy (XAS) [28], high-resolution multinuclear Solid State Nuclear Magnetic Resonance (SSNMR) spectroscopy [29], and multiscale classical reactive molecular dynamics simulations and quantum chemistry calculations [30]. We also show that Zr-Si mixed oxides are promising candidates as dehydrogenation catalysts to produce olefins.

2. Experimental

2.1. Materials synthesis

All the materials were previously synthesized via a sol-gel procedure and characterized via N_2 physisorption, X-ray Powder Diffraction (XRPD), and X-ray Photoemission Spectroscopy (XPS) [31]. The number of basic sites was determined by CO_2 physisorption (using an ASAP2020 instrument at 295 K), while pyridine adsorption monitored via Fourier Transform Infrared (FTIR) spectroscopy was used to determine the number and types of the acid sites [4]. Zirconyl chloride 30 % solution in HCl (Merck) and tetraethyl orthosilicate (Merck) were used as Zr and Si precursors, respectively. Depending on the intended Zr/Si molar ratio, a certain quantity of Zr precursor aqueous solution was added dropwise to an ammonia solution at a pH of 12. Then, a solution containing the Si precursor, isopropanol (Merck), and water (1:6:2 molar ratio, respectively) was added and stirred for three days at 75 °C. After washing with water until pH neutrality, the materials were calcined at 110 °C in the air overnight and at 350 °C for 4 hours (10 °C/min ramp rate), always in the air. The pure ZrO_2 material was prepared similarly, but to avoid any Si contamination from the glassware, PTFE containers were used instead. Three other materials at increasing content of Si were prepared and named according to their composition: ZrSi10, ZrSi30, and ZrSi50 (where the number refers to the weight percentage of SiO_2), representative of the Zr:Si molar ratios of 4:1, 1:1, and 1:2. Previously reported EDX analyses confirmed the intended compositional trend [4].

The same batch of ZrO_2 previously prepared was used for the sulfonation procedure [32]. 2 g of ZrO_2 were soaked in 30 mL H_2SO_4 (Merck) 1 N for two hours at room temperature. After filtration and washing with water, the solid was dried at 110 °C overnight in air and then calcined at 350 °C (10 °C/min) for four hours. The material was labeled $ZrSO_3H$.

The SiO_2-Al_2O_3 material (herein labeled as SiAl) was provided by Merck (specific surface area of 496 m^2/g).

2.2. Nitrogen physisorption isotherms

Nitrogen physisorption isotherms were collected with a Micromeritics ASAP2020 instrument. Prior to the analysis carried out at 77 K, the sample was first calcined at 350 °C in the air for 2 h and then treated under high vacuum at 200 °C for 2 h.

2.3. Transmission electron microscopy (TEM)

High Resolution Transmission Electron Microscopy analyses were collected with a ZEISS LIBRA200FE microscope equipped with a 200 kV FEG source. The samples were ultrasonically dispersed in isopropanol, and a drop of the obtained suspension was deposited on a holey-carbon film supported on a copper TEM grid of 300 mesh.

2.4. X-ray absorption spectroscopy (XAS)

Ex-situ XAS experiments were performed at the CATACT beamline [33] at the KIT Light Source in Karlsruhe, Germany. Powdered samples and reference materials were measured at the Zr K edge in transmission mode using the ionization chambers (OKEN Ltd, 800 V, Ar filled). The energy of the Si(311) double-crystal monochromator was calibrated by setting the first maximum of the first derivative of the XAS spectrum recorded on a Zr foil to the tabulated value of 17.998 keV. The samples were adequately diluted with cellulose and pressed into pellets before the measurements. Data processing was performed using the Athena package from the Demeter software [34]. The extended X-ray absorption fine structure (EXAFS) data were recorded up to $k = 16$ Å^{-1}. The EXAFS analysis was performed using the Artemis package from the Demeter software. The EXAFS data were Fourier transformed (FT) in the k range from 3.0 to 12.0 Å^{-1} using the Hanning window function with dk=1 Å^{-1} and are not phase corrected.

2.5. Diffuse reflectance fast Fourier infrared spectroscopy (DRIFTs)

The spectra were recorded with a BioRad FTS-60A after dehydrating the materials at 270 °C (20 min in the air + 20 min under vacuum).

2.6. Acidity measurements via Fourier transform infrared spectroscopy (FT-IR)

The acid features of $ZrSO_3H$ and SiAl were evaluated by pyridine adsorption using the same BioRad FTS-60A instrument. The experiments were performed on a sample disk (15–20 mg) after a dehydration treatment at 270 °C (20 min in air + 20 min under vacuum). A background spectrum prior to adsorption was obtained and subtracted from the subsequently recorded spectra. The adsorption of the probe molecule was carried out at room temperature, while the actual quantification was done after desorption at 120 °C to avoid pyridine decomposition [35] [36]. All the spectra were reported after being normalized by the disk weight.

2.7. Solid state nuclear magnetic resonance spectroscopy (SSNMR)

SSNNMR spectra were recorded on a Bruker Avance Neo spectrometer working at Larmor frequencies of ^{1}H, ^{29}Si, and ^{13}C nuclei of 500.13, 99.36, and 125.76 MHz, respectively, using a triple-resonance Magic Angle Spinning (MAS) probe head accommodating rotors with an external diameter of 2.5 mm. The 90-degree pulse duration was 2.1, 7.0, and 5.0 μs for ^{1}H, ^{29}Si, and ^{13}C nuclei, respectively. ^{29}Si MAS spectra were recorded at a MAS frequency of 7 kHz, under high-power decoupling from ^{1}H nuclei, using Cross Polarization (CP), with a contact time of 5 ms, a recycle delay of 4 s, and accumulating 5000–15000 transients. For ZrSi30, a ^{29}Si Direct Excitation (DE) spectrum was also recorded with a recycle delay of 180 s and 1280 transients. ^{1}H MAS spectra were recorded at a MAS frequency of 14 kHz, accumulating 16 transients. For ZrSi30, a ^{1}H–^{29}Si HETCOR spectrum was recorded, with FLSG decoupling during t1 [37]. Thirty-two increments were collected in the second dimension, with a dwell time of 37.9 μs, with 2 FSLG cycles per

increment. The ^{1}H rf field during FSLG was about 100 kHz. For each increment, 500 transients were accumulated. The ^{1}H MAS spectrum of ZrSi30 with Py-d_5 was recorded at a MAS frequency of 14 kHz, with an optimized recycle delay of 5 s and accumulating up to 1800 transients. The ^{13}C DE MAS spectrum of the same sample was recorded with a recycle delay of 5 seconds and accumulating 44640 transients. All the chemical shifts were referred to the ^{13}C peak of adamantane resonating at 38.46 ppm. All the spectra were recorded at 298 K. Deuterated pyridine (Py-d_5) vapors were adsorbed at room temperature on the ZrSi30 material using a vacuum line, followed by desorption at 120 °C. All rotors were packed in a glovebox under argon flux to avoid air exposure.

2.8. Molecular dynamics simulations

Reactive molecular dynamics simulations (RMD) of the growth process, based on the ReaxFF approach and a recent force field appropriately developed for these types of materials [38], were carried out by filling cubic simulation boxes with Zr, Si, and O atoms randomly, considering the experimental density of the final materials. The simulations were performed in the NVT ensemble at high temperatures to speed up the aggregation process. In all the RMD runs, the time step was set to 0.5 fs, and the temperature was controlled through the Hoover-Nosé thermostat with a relaxation constant of 0.1 ps. RMDs were carried out with the ReaxFF code implemented in the Lammps package [39]. The systems structures were collected every picosecond. The total simulation time was between 2 and 5 ns for the different stoichiometries. The trajectories were analyzed to extract the final values of surface areas and pore volume using the PoreBlazer software [40]and to extract size-reduced systems for the quantum chemistry (QC) calculations.

2.9. QC calculations

All the DFT calculations were performed with the Quantum Espresso (QE) suite of programs [41], employing PAW (Plane-Augmented-Waves) pseudopotentials, the PBE-D2 XC-functional [42] [43], and plane-waves as basis sets to build Bloch states. Cut-offs on the wave function and electronic density were set to 40/400 Ry (1 Ry = 313.8 Kcal/mol), and the first Brillouin cell in the reciprocal space was sampled at the Gamma point only (non-periodic system). Calculations were performed spin-restricted by applying Gaussian smearing of the one-particle energy levels of 0.002 Ry. NMR Chemical Shifts (CS) were simulated by using the GIPAW approach [44] implemented in QE.

2.10. Dehydration reaction of 1-octanol

The tests were carried out in a flow setup using a stainless-steel reactor (4 mm internal diameter). Before each test, the materials were treated for 40 mins at 270 °C (10 °C/min ramp rate) in a 40 mL/min N_2 flow. An HPLC pump delivered the 1-octanol to the reactor. The reaction products were identified via a GC-MS instrument (Agilent, 7890 A) and then quantified with a GC-FID instrument (Agilent, 6890) using hexadecane as standard. In both cases, an HP5 column was used. The catalytic activity was evaluated at 325 °C by adjusting the liquid hourly space velocity (LHSV), calculated as the ratio of the 1-octanol flow rate over the catalytic bed volume, between 9 and 18 h^{-1} to start the test at about the same conversion level of 80–90 % with all the materials examined. The olefins productivity data are reported as Space Time Yield, defined as moles of olefins per hour per gram of catalyst.

3. Results and discussion

A series of Zr-Si mixed oxides were prepared using a conventional sol-gel procedure to obtain amorphous materials featuring a high dispersion of both Zr and Si. These materials were already used for other applications and characterized in their main compositional and acid/base characteristics [4,31]. We focused our attention on the ZrSi30 sample, whose Zr:Si molar ratio is 1:1, because it displayed the highest number of Brøsted acid sites (Fig. 1). The XRPD analyses did not show any diffraction peak, thus confirming its amorphous nature (Figure S1). The other two mixed oxide samples, with Zr:Si molar ratios of 4:1 (ZrSi10) and 1:2 (ZrSi50), were prepared as representatives of systems featuring an excess of Zr and Si, respectively.

The acid/base characteristics of the materials are summarized in Fig. 1, while the FTIR pyridine desorption spectra are shown in Figure S2. Starting from the pure ZrO_2, which has both acidic (only Lewis) and basic sites, increasing the amount of Si, the latter progressively disappear while BAS appear. ZrSi30 has the highest number of BAS and retains more Lewis acid sites than ZrSi50. As it will be discussed later, the drop in the acidic characteristics of ZrSi50 could be related to the decrease in specific surface area and the more silica-like composition (Figure S3).

We started this investigation by developing morphological models. Consistently with the experimental density of 0.808 g/cm^3, particle-growing computational protocol exploiting ReaxFF Molecular Dynamics (MD) simulations produced several models with stoichiometric ZrSi30 composition by tuning the simulation temperature (in the range 1000 – 2000 K), the box size (98 Å, corresponding to 2500 Zr, 2500 Si and 10,000 O atoms or 123 Å, corresponding to 5000 Zr, 5000 Si, and 20,000 O atoms), and the hydrogen content (from 0 % to 100 % relative to the total number of Zr and Si atoms in the simulation box). The most representative morphologies are shown in Fig. 2.

Fig. 2(a) shows that ZrSi30 corresponds to the maximum surface area (around 350 m^2/g) with a pore diameter of about 6 nm. But, as seen from the HRTEM micrograph in Fig. 2(b), ZrSi30 is made of tightly packed particles of 5–7 nm. Comparing the HRTEM, BET data, and theoretical models, the porosity revealed by the N_2 adsorption isotherms can be linked to the interparticle distance originating from the aggregation of the particles. When simulating the growth process at high temperature (2000 K), we achieved a periodic array of agglomerated nanoparticles with dimensions in the 6–8 nm range, an average distance of about 7 nm, and a surface area of 360 m^2/g. As shown in Fig. 2(c), the average distance between the particles (about 7 nm) was in satisfactory agreement with the experimental measurements.

On the contrary, at lower growth temperatures, the final morphology shown in Fig. 2(d) is sparser, displaying a larger surface area (about 1300 m^2/g) and pores of about 2 nm. It is worth mentioning that neither the size of the unit cell nor the hydrogen content affected the final morphology. Systems with the ZrSi50 and ZrSi10 stoichiometries were generated through an analogous procedure.

XAS analysis provided detailed information on the Zr environment.

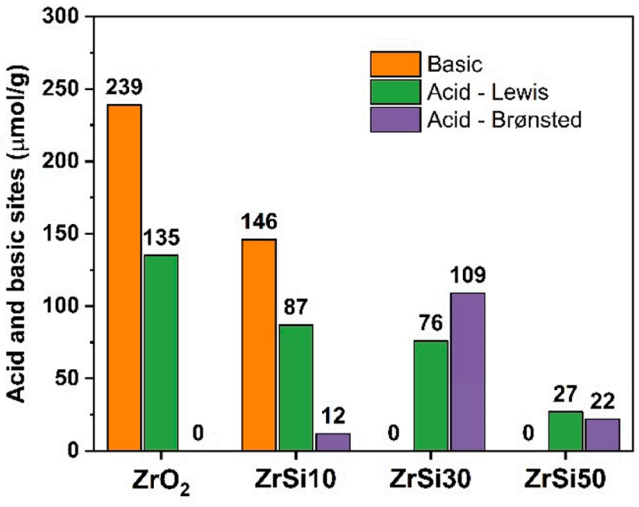

Fig. 1. The acid/base characteristics of the Zr-Si mixed oxides here studied. Adapted from Ref. [4].

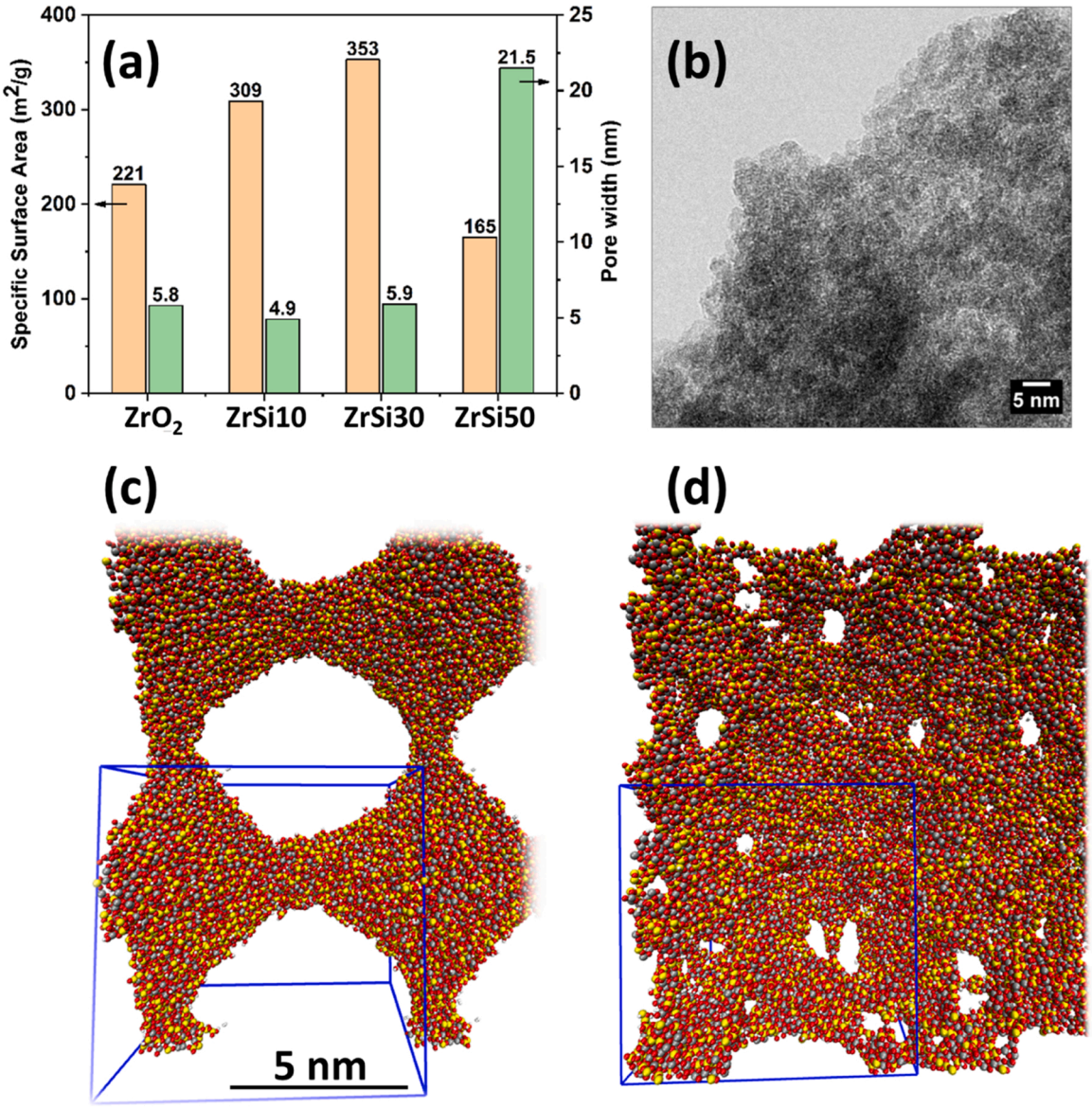

Fig. 2. (a) Experimental specific surface area and pore width of the synthesized ZrO_2, ZrSi10, ZrSi30, and ZrSi50 [4]. (b) Representative HRTEM micrograph of ZrSi30. The final morphology of simulations adopted cubic boxes with a side of 98 Å and containing 2500 Zr, 2500 Si, 10,000 O, and 2500 H atoms. Simulation temperatures were 2000 K in (c) and 1000 K in (d). O atoms are depicted as red balls, Si as yellow balls, Zr as grey balls, and H as white balls. The simulation box (blue lines) is displayed in panels (c) and (d). (For interpretation of the references to color in this figure legend, the reader is referred to the web version of this article.)

The general shape of the Zr K X-ray absorption near edge structure (XANES) spectra of zirconium oxide (Fig. 3(a)) is relatively well understood. The local symmetry of *3d* states influences the pre-edge at around 18,003 eV in the ZrO_x coordination complex, while the main absorption feature at 18,022 eV reflects the chemical bonding between Zr *4 s* and O *2p* states [45]. The typical single absorption features for the m-ZrO_2 (baddeleyite phase) with seven-fold Zr coordinated to O in our ZrO_2 sample split into a double-peaked structure (peaks II at 18,020 eV and III at 18,029 eV in Fig. 3). This, together with the formation of a more pronounced pre-edge feature (peak I), is proposed to be a sign of significant tetragonal distortion in ZrO_x characterized by eight-coordinated Zr with the Zr-O bonds longer than in baddeleyite, like in stabilized zirconia, or might be a hint to the presence of six-coordinated Zr with shorter Zr-O bonds [46,47]. The analysis of the extended X-ray absorption fine structure (EXAFS) data (Fig. 3(b) and Table S1) revealed a decrease in the average coordination number of O and Zr (peaks at 1.7 Å and 3.1 Å, respectively) and a shortening of the Zr-O bond in both pure ZrO_2 and ZrSi30 samples compared to m-ZrO_2. No long-term order was found (see the low intensity of the peaks at distances above 3.5 Å in Fig. 3(b)), in agreement with the morphological observations [4,31] (Fig. 2). The proposal that the ZrO_6 units are homogeneously distributed in the solid matrix without building large zirconia particles is thus further supported. For pure Zr oxides, the reduced Zr-O coordination number, the shorter Zr-O bonds, and the change of shape of the XANES spectra hint at the formation of octahedrally coordinated Zr^{4+} stabilized by linkages with SiO_4 in ZrSi30 [45,48].

The formation of direct Zr-Si bonds can be excluded as no Zr-Si peak at about 2.25 Å (like in $ZrSi_2$, not shown here) is present in the FT EXAFS data (Fig. 3(b)). Zr-Si bonds had been assigned to the peak at about 3 Å [48], but this is unlikely since the same peak can be found in the spectrum of pure ZrO_2. The formation of Zr-O-Si bonds is, hence, more realistic and will be verified experimentally via FT-IR and SSNMR spectroscopies.

Indeed, analyzing the skeletal vibrational region in the FTIR spectra

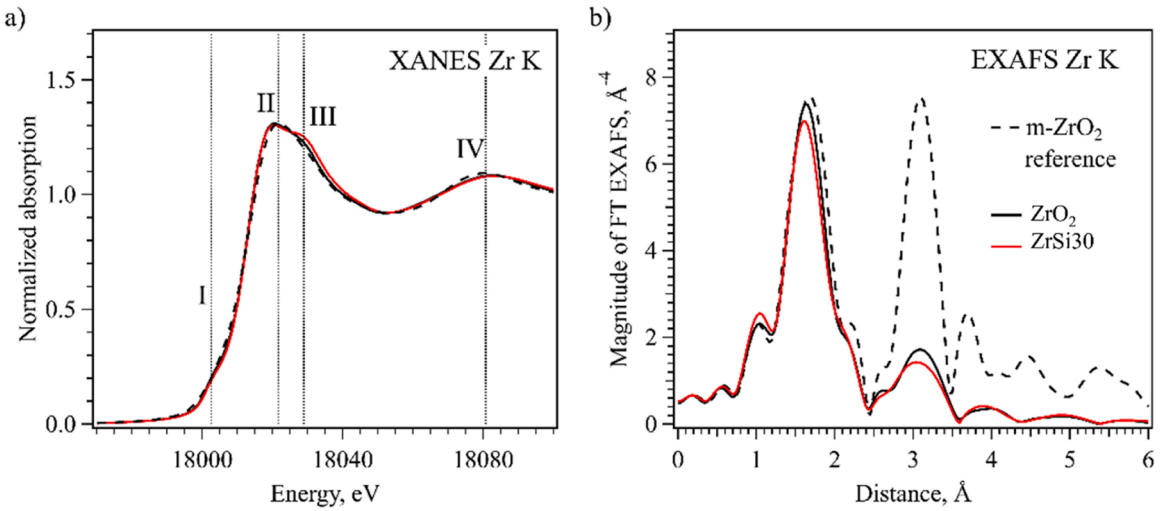

Fig. 3. (a) Normalized Zr K XANES spectra and (b) magnitude of Fourier transformed k_3-weighted EXAFS spectra, not phase corrected, of the ZrO_2 and ZrSi30 samples along with the reference material (m-ZrO_2, baddeleyite phase).

shown in Fig. 4, the presence of Zr-O-Si bonds can be confirmed in all the Zr-Si mixed oxides by the bands located at around 1115–1166 cm^{-1} [49]. The bands around 760 cm^{-1} and 1060 cm^{-1} are typical of Si-O bonds; the band at about 1200 cm-1 is visible only in the spectrum of ZrSi50, which reflect the higher Si content of this material and a more silica-like structure[17,50].

Another proof of the presence of the Zr-O-Si bond is provided by ^{29}Si SSNMR spectra, shown in Fig. 5(a). The spectra show a broad peak, whose maximum progressively shifts towards lower chemical shifts (from −88 ppm of ZrSi10 to −100 ppm of ZrSi50) with increasing the content of Si. This effect has been already ascribed to the formation of Zr-O-Si linkages in mixed oxides [48,51] [52,53]. The broad peak observed agrees with the amorphous nature of these materials and arises from a distribution of different species and bond lengths and angles. On the other hand, the regular trend of the chemical shift of the maximum of the peak suggests a progressive increase of Zr to Si substitution with increasing the Zr/Si ratio, associated with an intimate and homogeneous mixing of Si and Zr atoms. In particular, considering that the substitution of Si with Zr is reported to induce a shift of about +5 ppm, the values of the ^{29}Si chemical shift measured at the maximum of the peak suggest the formation of the following main species: $Si(OSi)_3(OH)$ and $Si(OSi)_2(OZr)(OH)$ in ZrSi50, $Si(OSi)_2(OZr)(OH)$ and $Si(OSi)(OZr)_2(OH)$ in ZrSi30 and $Si(OSi)(OZr)_2(OH)$ and $Si(OZr)_3(OH)$ in ZrSi10, in excellent agreement with samples stoichiometry. It must be mentioned that these spectra were recorded by Cross Polarization (CP) from ^{1}H to ^{29}Si nuclei, thus favoring silicon atoms bearing OH groups, presumably more

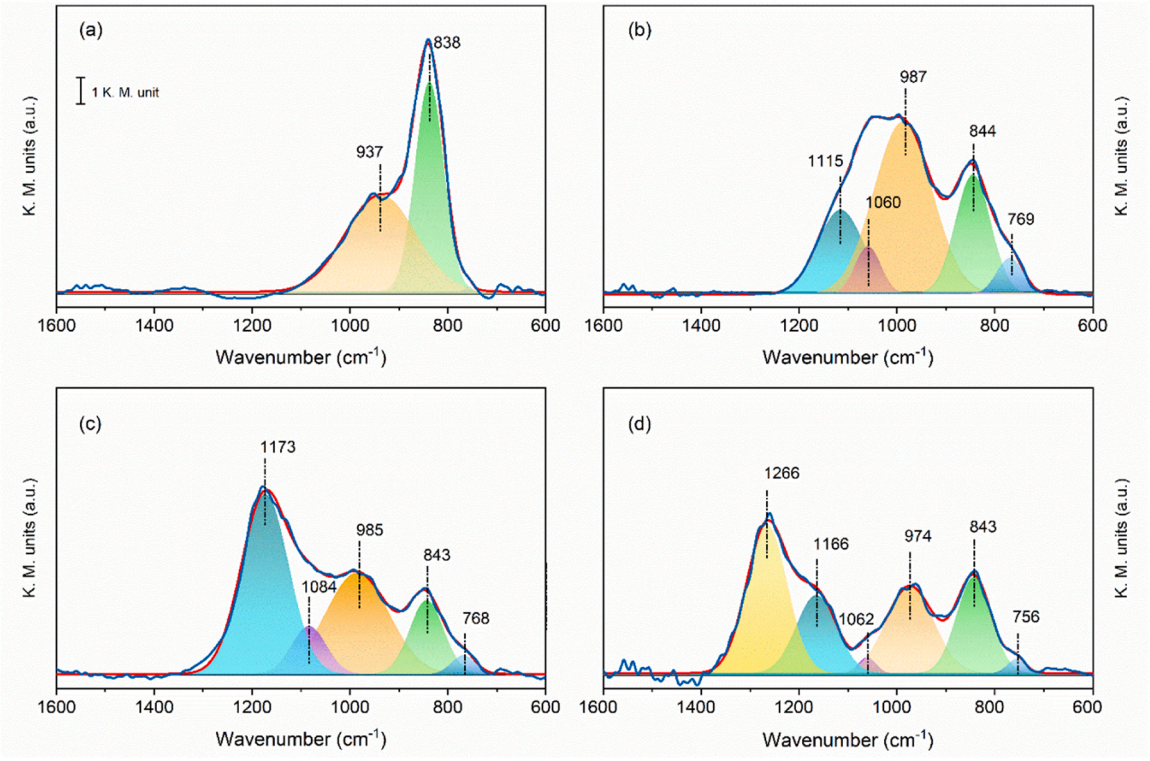

Fig. 4. DRIFTs spectra with peaks deconvolution of (a) ZrO_2, (b) ZrSi10, (c) ZrSi30, and (d) ZrSi50.

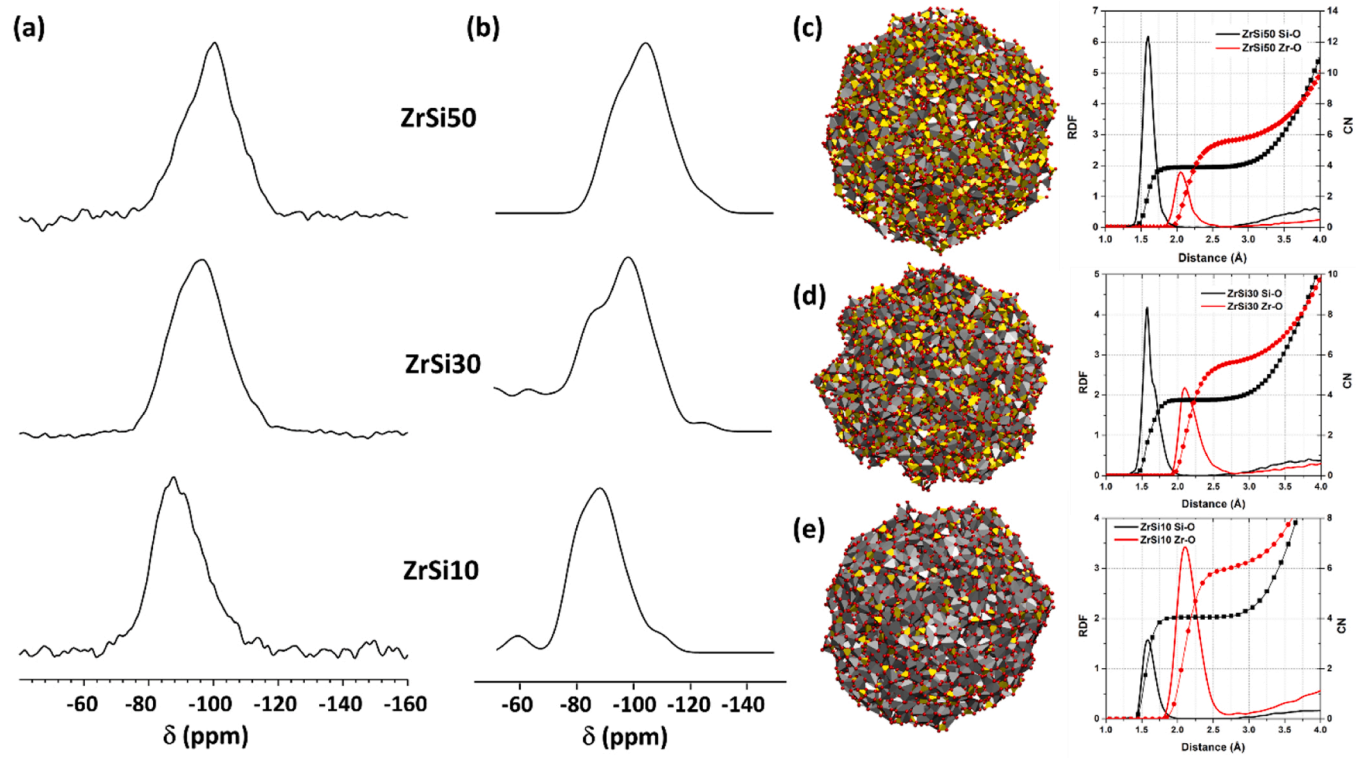

Fig. 5. (a) Experimental ^{1}H–^{29}Si CP MAS SSNMR spectra of the indicated samples (b) GIPAW-simulated ^{29}Si MAS SSNMR spectra of the three nanoparticles with composition (c) ZrSi50, (d) ZrSi30 and (e) ZrSi10 achieved with modeling. On the right, the relative RDF (Radial Distribution Function) and CN (Coordination Number) of Si-O (black data) and Zr-O (red data) are shown. The polyhedral representations of the nanoparticles include Si (yellow) and Zr (grey) areas, whereas O atoms are rendered as red balls. The three nanoparticles have an average diameter of about 6 nm.

abundant at the materials surface. The quantitative Direct Excitation (DE-MAS) spectrum of ZrSi30 (Figure S4) better highlights also the presence of $Si(OSi)_2(OZr)_2$ species, resonating at a chemical shift of about −100 ppm.

To obtain more detailed information on the structure of the investigated samples, by applying the computational growth parameters derived for the morphological models of the aggregated nanoparticles shown in Fig. 2(c), we derived the structures of three isolated nanoparticles, with the desired ZrSi10, ZrSi30, and ZrSi50 stoichiometries, shown in Fig. 5(c-e). From a detailed structural analysis, neither ordered

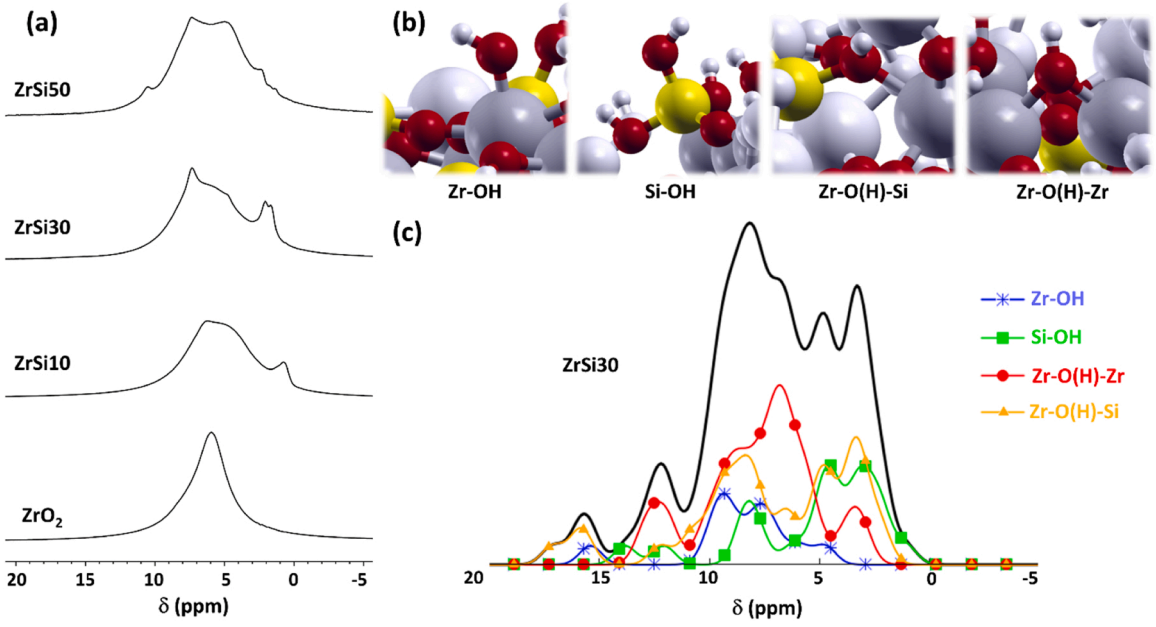

Fig. 6. (a) Experimental ^{1}H MAS SSNMR spectra of all the indicated samples. (b) Four different categories of surface -OH groups: from left to right, -OH on top of Zr atoms (Zr-OH), -OH on top of Si atoms (Si-OH), bridge -OH between one Zr and one Si atom (Zr-O(H)-Si), and bridge -OH between two Zr atoms (Zr-O(H)-Zr). O, Si, Zr, and H are rendered with red, yellow, grey, and white balls, respectively. (c) GIPAW-simulated chemical shifts of a selection of protons from the surface of the ZrSi30 nanoparticle: the total signal (black line) is decomposed according to the topology of the different -OH groups reported in (b).

crystal regions nor Zr-Si bonds in such nanoparticles were found. Most Si atoms are tetracoordinate (black curves corresponding to the integrated RDF of the Si-O bonds in Fig. 5). In contrast, the coordination of most of the Zr atoms is close to six (red curves corresponding to the integrated RDF of the Zr-O bonds in Fig. 5), in agreement with EXAFS data. These results also agree with those reported by Sheikholeslam et al. [54], who investigated mixed Zr-Si bulk oxides at low Zr content via a similar computational growth protocol employing ReaxFF.

Furthermore, by using reduced surface models of the larger aggregates, according to a procedure detailed in the Supplementary Material and analog to that outlined by Caricato [52], we were able to simulate, at the DFT level, the ^{29}Si SSNMR chemical shift of a random ensemble of surface silicon atoms (see Fig. 5(b)): the agreement with the experimental spectra in Fig. 5(a) is excellent. Further details on the procedure used to derive the reduced models and simulated spectra are reported in the Supplementary Material.

As BAS are hydroxide groups, we then recorded ^{1}H SSNMR spectra (Fig. 6(a)). The spectrum of pure ZrO_2 allowed the identification of the signal arising from Zr-OH groups, which has a maximum at 6 ppm and a shoulder at about 8 ppm [55]. The spectra of the mixed Zr-Si samples are characterized by a relatively broad and barely resolved distribution of signals, spanning the region 1–12 ppm, with some local intensity maxima at 1.5, 2.0, 4.7, 7.2, and 10.5 ppm. The low resolution can be mainly ascribed to a distribution of isotropic chemical shifts, as confirmed by the failure of CRAMPS experiments. These spectra are quite peculiar compared to the few reported in the literature for Zr-Si mixed oxides [53,56], and an analysis of variable compositions has not been reported yet. A tentative assignment of the observed signals can be proposed, but, as it will be evident in the following, the structural complexity and disorder of these materials and the sensitivity of the ^{1}H chemical shifts to minor variations of the local environment of H atoms, make crucial and beneficial the combination of the experimental data with modeling predictions. The signals at 1.5 and 2 ppm were repeatedly observed in zeolites and ascribed to isolated Si-OH groups, both not involved in H bonds but having a non-acidic and acidic character, respectively [29,56,57]. All the other H nuclei are expected to contribute to the broad signal at chemical shifts higher than 2 ppm. We also recorded a ^{1}H–^{29}Si 2D HETCOR spectrum of ZrSi30 (Figure S6), which showed cross-peaks between the ^{29}Si signal and all ^{1}H signals below 10 ppm.

The reduced cluster models from the ZrSi30 NP of Fig. 5(d) used to simulate ^{29}Si chemical shifts were also used to simulate ^{1}H CS at the same level of theory, refine the data collected from the SSNMR experiments and speculate on the nature of surface -OH groups. The following classification, displayed in Fig. 6(b), was obtained: -OH on top of Zr atoms (Zr-OH), -OH on top of Si atoms (Si-OH), bridge -OH between one Zr and one Si atom (Zr-O(H)-Si), and bridge -OH between two Zr atoms (Zr-O(H)-Zr). No bridged -OH between two Si atoms was singled out, in agreement with the results of FT-IR analyses, which evidenced Si-O-Si bands only in the spectrum of the ZrSi50 system (Fig. 4). The decomposition in terms of the four groups of -OH atoms of the spectra simulated via DFT allowed the definition of the contribution of each -OH group to the overall spectrum, as depicted in Fig. 6(c). The comparison between the experimental and the cumulative simulated ^{1}H spectrum is excellent, confirming the reliability of the derived structural models.

As per tradition, while probing the acidity of materials [35,36], pyridine adsorption was carried out experimentally in its perdeuterated form (Py-d_5) and examined via SSNMR. The ^{1}H MAS spectrum of ZrSi30 exposed to Py-d_5 (Fig. 7(b)), compared with that of ZrSi30 (Fig. 7(a)), shows an intensity decrease for the signals at 2 and 4.7 ppm and a corresponding increase at 7 ppm. The peak at very high chemical shift (12–16 ppm) often observed for the pyridinium ion in zeolites is not observed [58–61], suggesting that there is a fast hydrogen exchange between surface acidic sites and Py-d5, resulting in an average ^{1}H NMR spectrum. This was confirmed by the ^{13}C spectrum of Py-d_5 (Fig. 7(c)). The ^{13}C chemical shifts observed here correspond to those reported for C_α, C_γ (peak at 145 ppm), and C_β (peak at 125 ppm) for pyridinium and pyridine in 0.6 molar ratio, rapidly exchanging with a characteristic time less than 10^{-3} s [62]. This number fits very well with the molar ratio between the number of BAS and the total amount of acid sites, 0.59, in our ZrSi30 material (Fig. 1). It is worth noticing the decrease in the intensity at about 2 and 4.7 ppm in the ^{1}H MAS spectrum of ZrSi30 after Py-d_5 adsorption, which suggests that the sites mainly affected by the pyridine adsorption are those where the -OH groups are on top of Si and/or bridged between Si and Zr. To precisely untangle the many

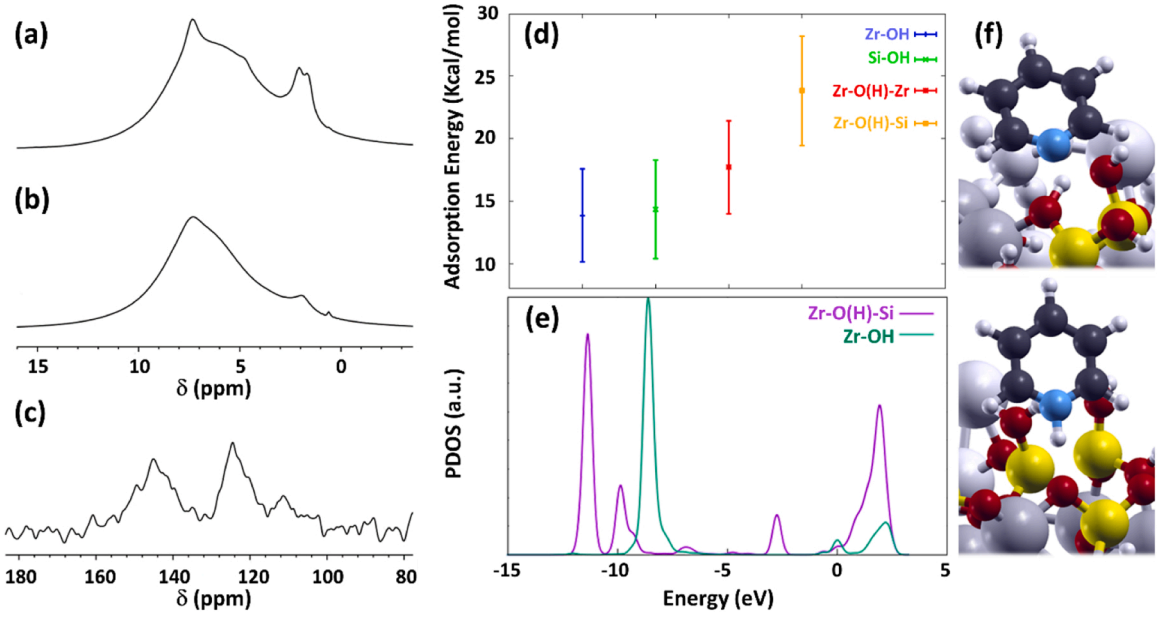

Fig. 7. ^{1}H MAS SSNMR spectrum of ZrSi30 before (a) and after (b) adsorption of Py-d_5; (c) ^{13}C DE MAS SSNMR spectrum of Py-d_5 adsorbed on ZrSi30. (d) Adsorption energy of the pyridine molecule interacting with four -OH of the surface of the ZrSi30 nanoparticle. (e) Projected Density of States corresponding to the 1 s function of two different H atoms on the ZrSi30 nanoparticle surface: an oxidized H atom (purple) corresponding to a bridge Zr-O(H)-Si and a top Zr-OH (green). (f) Proto-typical example of proton extraction from a bridge Zr-O(H)-Si site corresponding to the formation of a pyridinium ion. (For interpretation of the references to color in this figure legend, the reader is referred to the web version of this article.)

contributions to this part of the spectrum, we estimated the adsorption energy of pyridine on the most exposed surface H atoms by performing a constrained local optimization of the atoms of pyridine along with the O and H atoms of the surface in direct contact with it (Fig. 7(d)) [60]. Regardless of the relatively wide error bars due to the inherent heterogeneity of the system, the trend is clear and indicates that pyridine interacts more strongly with an -OH group bridged between Zr and Si atoms (Zr-O(H)-Si). Interestingly, in more than 90 % of the sampled sites, the adsorption of pyridine was accompanied by the direct extraction of the sampled proton and the formation of a pyridinium ion, as explicitly shown in Fig. 7(f). The Projected Density of States (Fig. 7(e)), derived from the DFT simulation on a typical cluster model, showed that the H atom of the bridged Zr-O(H)-Si group is more oxidized, and hence characterized by a larger percentage of its wave function above the Fermi level, than that, for instance, in the on-top configuration Zr-OH. This is coherent with the pronounced tendency of the bridged Zr-O(H)-Si to exhibit Brønsted character via the direct protonation of the pyridine in contact with it. It can be noted that the change of the ^{1}H MAS spectrum of ZrSi30 exposed to Py-d_5 (Fig. 7(a) *vs* Fig. 7(b)) is consistent with this picture, as the contribution deriving from Zr-O(H)-Si, although quite broadened in the region from 1 to 10 ppm, has a significant weight in the region below 5 ppm, where it is dominant together with the contribution deriving from Si-OH. Reasonably, in the region between 5 and 10 ppm, a decrease of the contribution from Zr-O(H)-Si is less evident in the overall spectrum, due to the strong weight played by H species in Zr environment.

Finally, the ZrSi30 material was tested in the dehydration reaction of 1-octanol in flow conditions against two other reference materials featuring BAS, namely a sulfonated zirconia ($ZrSO_3H$) prepared by us starting from the same ZrO_2 batch and a commercial acidic silica-alumina (SiAl). The total acidity profiles of all these materials are reported in Figure S7. These tests allowed us to showcase the potential of ZrSi30 as a catalyst to produce olefins, particularly from long-chain alcohols, which are of interest for the elastomer industry [63] and, more recently, for the production of sustainable jet fuels [64]. The results are displayed in Fig. 8. It can be observed that not only ZrSi30 is far more stable than the other two materials as far as the overall olefin productivity, but it also showed the highest selectivity toward 1-octene, which is the most valuable among the isomers and the lowest toward the ether. Such high and constant selectivity of ZrSi30 is consistent with the well-balanced BAS and LAS of this material (Figure S7), as already reported for other solid acid catalysts in alcohol dehydration reactions [65,66]. The overall stability of ZrSi30 can be ascribed to two factors. Firstly, the low quantity and easy-to-burn-off carbonaceous deposits found after the reaction by thermogravimetric analyses (Figure S8). Secondly, ZrSi30 retained its morphological characteristics practically unaltered, i.e., surface area and porosity along with the N_2 isotherm shape, as evidenced by the comparison between the fresh and used material in Figure S9 and Table S3. These data confirm that it is possible to obtain in a simple manner a highly acidic and robust Zr-based catalyst that outperforms even Si-Al mixed oxides by simply playing with their composition while avoiding harsh treatments with mineral acids.

4. Conclusions

In summary, the results presented here allowed us to collect strong indications pointing towards -OH groups bridging Zr and Si atoms (Zr-O(H)-Si) (see Fig. 6(b)) as the Brønsted acid sites characterizing amorphous Zr-Si mixed oxides at 1:1 composition. Such a conclusion was achieved via an intertwined approach exploiting a combination of experimental and theoretical techniques. Working on a series of materials covering a wide range of compositions, the proposed multi-technique approach allowed the identification of agglomerated nanoparticles with amorphous morphology and a Brønsted acidity characterized by a typical volcano profile in favor of ZrSi30 composition. Atomistic multiscale modeling was used to provide possible structural models of the nanoparticles that were coherent with the experimental data, namely qualitative coherence with the EXAFS and SSNMR spectra. Pyridine adsorption analyses identified the surface BAS. We could estimate the pyridine adsorption energy by screening surface OH groups with different topologies, and the OH group bridging Zr and Si atoms was the most acidic one. Finally, ZrSi30 was tested against some reference materials featuring BAS in the dehydration reaction of 1-octanol in flow conditions. The results showed that the ZrSi30 material outperforms the others in terms of stability and selectivity to 1-octene, which is the most valuable isomer for critical industrial processes like elastomer production. We can conclude this paper by stressing two aspects: the first is related to the ZrSi30 material, which proved to be an

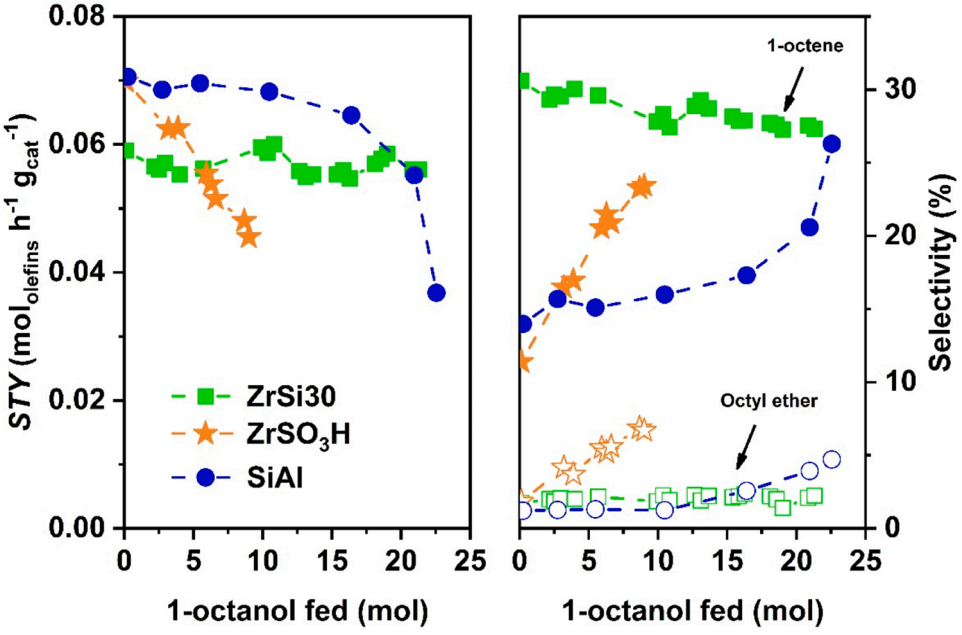

Fig. 8. Catalytic dehydration reactions of 1-octanol at 325 °C. Olefins space time yield (left) and selectivity (right) toward 1-octene (solid) and octyl ether (empty). The space velocity was adjusted between 9 and 18 h^{-1} to start the tests at a comparable initial conversion level of 80–90 %.

excellent catalyst material potentially able to attract industrial interest; secondly, we showed how only an approach based on an intertwined multi-technique characterization can shed light on the complex morphology and structure/property relationships of highly amorphous materials, such as the mixed Zr-Si oxide nanoparticles presented here. In perspective, this multi-characterization-technique approach could help accelerate the knowledge-based development of high-performance industrial relevant materials.

CRediT authorship contribution statement

Anna Zimina: Writing – review & editing, Writing – original draft, Investigation, Formal analysis, Data curation. **Susanna Monti:** Writing – review & editing, Writing – original draft, Software, Methodology, Investigation, Data curation, Conceptualization. **Silvia Borsacchi:** Writing – review & editing, Writing – original draft, Visualization, Investigation, Formal analysis, Data curation, Conceptualization. **Nicola Scotti:** Writing – review & editing, Methodology, Investigation, Formal analysis. **Marco Geppi:** Methodology, Investigation, Formal analysis, Data curation. **Claudio Evangelisti:** Writing – review & editing, Writing – original draft, Methodology, Investigation, Formal analysis, Conceptualization. **Paolo Dambruoso:** Investigation, Formal analysis. **Nicoletta Ravasio:** Investigation, Conceptualization. **Vladimiro Dal Santo:** Investigation. **Filippo Bossola:** Writing – review & editing, Writing – original draft, Methodology, Investigation, Formal analysis, Data curation, Conceptualization. **Giovanni Barcaro:** Writing – review & editing, Writing – original draft, Software, Investigation, Data curation, Conceptualization.

Declaration of Competing Interest

The authors declare that they have no known competing financial interests or personal relationships that could have appeared to influence the work reported in this paper.

Data availability

Data will be made available on request.

Acknowledgements

We acknowledge the Institute of Beam Physics and Technology (IBPT) for operating the storage ring, the Karlsruhe Research Accelerator (KARA).

The Center for Instrument Sharing of the University of Pisa (CISUP) is acknowledged for the availability of the Solid State NMR instrumentation.

We acknowledge Mr. Roberto Spiniello (CNR-ICCOM) for the thermogravimetric analyses carried out on the used catalysts.

Appendix A. Supporting information

Supplementary data associated with this article can be found in the online version at doi:10.1016/j.jallcom.2024.174545.

References

[1] K. Tanabe, T. Yamaguchi, Acid-base bifunctional catalysis by ZrO2 and its mixed oxides, Catal. Today 20 (2) (1994) 185–197, https://doi.org/10.1016/0920-5861(94)80002-2.

[2] H.H. Kung, Formation of new acid sites in dilute oxide solid solutions: a predictive model, J. Solid State Chem. 52 (2) (1984) 191–196, https://doi.org/10.1016/0022-4596(84)90191-9.

[3] C.L. Thomas, Chemistry of Cracking Catalysts, Ind. Eng. Chem. 41 (11) (1949) 2564–2573, https://doi.org/10.1021/ie50479a042.

[4] F. Zaccheria, F. Bossola, N. Scotti, C. Evangelisti, V. Dal Santo, N. Ravasio, On demand production of ethers or alcohols from furfural and HMF by selecting the composition of a Zr/Si catalyst, Catal. Sci. Technol. 10 (22) (2020) 7502–7511, https://doi.org/10.1039/D0CY01427C.

[5] H.J.M. Bosman, E.C. Kruissink, J. van der Spoel, F. van den Brink, Characterization of the acid strength of SiO2-ZrO2 mixed oxides, J. Catal. 148 (1994) 660–672.

[6] K. Tanabe, S. Takashi, S. Katsue, K. Tadamitsu, K. Jun, A new hypothesis regarding the surface acidity of binary metal oxides, Bull. Chem. Soc. Jpn. 47 (5) (1974) 1064–1066, https://doi.org/10.1246/bcsj.47.1064.

[7] L. Hu, L. Lin, Z. Wu, S. Zhou, S. Liu, Chemocatalytic hydrolysis of cellulose into glucose over solid acid catalysts, Appl. Catal. B Environ. 174–175 (2015) 225–243, https://doi.org/10.1016/j.apcatb.2015.03.003.

[8] M.D. Rhodes, K.A. Pokrovski, A.T. Bell, The effects of zirconia morphology on methanol synthesis from CO and H 2 over Cu/ZrO2 catalysts: part II. Transient-response infrared studies, J. Catal. 233 (1) (2005) 210–220, https://doi.org/10.1016/j.jcat.2005.04.027.

[9] W. Zhang, Z. Wang, J. Huang, Y. Jiang, Zirconia-based solid acid catalysts for biomass conversion, Energy Fuels 35 (11) (2021) 9209–9227, https://doi.org/10.1021/acs.energyfuels.1c00709.

[10] J. Wei, et al., Highly Efficient reductive etherification of 5-hydroxymethylfurfural to 2,5-bis(alkoxymethyl)furans as biodiesel components over Zr-SBA catalyst, Energy Technol. 7 (5) (2019) 1–11, https://doi.org/10.1002/ente.201801071.

[11] N. Scotti, F. Bossola, F. Zaccheria, N. Ravasio, Copper–zirconia catalysts: powerful multifunctional catalytic tools to approach sustainable processes, Catalysts 10 (2) (2020) 168, https://doi.org/10.3390/catal10020168.

[12] H.K. Min, et al., Phase transformation of ZrO2 by Si incorporation and catalytic activity for isopropyl alcohol dehydration and dehydrogenation, Chem. Eng. J. 428 (2022) 131766, https://doi.org/10.1016/j.cej.2021.131766.

[13] H. Li, et al., Conversion of ethanol to 1,3–butadiene over Ag–ZrO2/SiO2 catalysts: the role of surface interfaces, J. Energy Chem. 54 (2020) 7–15, https://doi.org/10.1016/j.jechem.2020.05.038.

[14] N. Scotti, F. Zaccheria, C. Evangelisti, R. Psaro, N. Ravasio, Dehydrogenative coupling promoted by copper catalysts: a way to optimise and upgrade bio-alcohols, Catal. Sci. Technol. 7 (6) (2017) 1386–1393, https://doi.org/10.1039/c6cy02670b.

[15] S. Kumaravel, et al., Highly selective catalytic transfer hydrogenation of biomass derived furfural to furfural alcohol over Zr/SBA-15 catalysts, J. Phys. Chem. Solids 186 (2024) 111831, https://doi.org/10.1016/j.jpcs.2023.111831.

[16] S. Pyen, E. Hong, M. Shin, Y.W. Suh, C.H. Shin, Acidity of co-precipitated SiO2-ZrO2 mixed oxides in the acid-catalyzed dehydrations of iso-propanol and formic acid, Mol. Catal. 448 (2018) 71–77, https://doi.org/10.1016/j.mcat.2018.01.031.

[17] J.A. Anderson, C. Fergusson, I. Rodríguez-Ramos, A. Guerrero-Ruiz, Influence of Si/Zr ratio on the formation of surface acidity in silica-zirconia aerogels, J. Catal. 192 (2) (2000) 344–354, https://doi.org/10.1006/jcat.2000.2850.

[18] J.B. Miller, E.I. Ko, Acidic properties of silica-containing mixed oxide aerogels: preparation and characterization of zirconia-silica and comparison to titania-silica, J. Catal. 159 (1) (1996) 58–68, https://doi.org/10.1006/jcat.1996.0064.

[19] Q. Wang, Wenlei Xie, L. Guo, Molybdenum and zirconium oxides supported on KIT-6 silica: a recyclable composite catalyst for one–pot biodiesel production from simulated low-quality oils, Renew. Energy 187 (2022) 907–922, https://doi.org/10.1016/j.renene.2022.01.122.

[20] M. Boronat, A. Corma, Factors controlling the acidity of zeolites, Catal. Lett. 145 (1) (2015) 162–172, https://doi.org/10.1007/s10562-014-1438-7.

[21] M. Kawai, M. Tsukada, K. Tamaru, Surface electronic structure of binary metal oxide catalyst ZrO2/SiO2, Surf. Sci. 111 (2) (1981), https://doi.org/10.1016/0039-6028(80)90701-3.

[22] Y. Shen, A new hypothesis of micro-region acid sites regarding the surface acidity of binary oxides, RSC Adv. 2 (14) (2012) 5957–5960, https://doi.org/10.1039/c2ra20184d.

[23] I.A. Fisher, A.T. Bell, A mechanistic study of methanol decomposition over Cu/SiO2, ZrO2/SiO2, and Cu/ZrO2/SiO2, J. Catal. 184 (2) (1999) 357–376, https://doi.org/10.1006/jcat.1999.2420.

[24] J.B. Miller, E.I. Ko, Control of PRehydrolysis Ratio for Sol-gel Preparation of Homogeneous Zirconia-silica Aerogels, J. Catal. 153 (1) (1995) 194–196, https://doi.org/10.1006/jcat.1995.1121.

[25] Y. Ma, et al., Slurry-phase hydrocracking of a decalin-phenanthrene mixture by MoS2/SiO2-ZrO2 bifunctional catalysts, Ind. Eng. Chem. Res. 60 (1) (2021) 230–242, https://doi.org/10.1021/acs.iecr.0c04999.

[26] N. Peddinti, P.C. Venkata, P. Challa, D.R. Burri, S.R.R. Kamaraju, Vapor phase selective production of ethyl lactate over ZrO2-SiO2 catalysts using lactic acid and ethanol, ChemistrySelect 3 (39) (2018) 10843–10848, https://doi.org/10.1002/slct.201801740.

[27] B. Li, R.D. Gonzalez, The effect of coke deposition on the deactivation of sulfated zirconia catalysts, Appl. Catal. A Gen. 174 (1–2) (1998) 109–119, https://doi.org/10.1016/S0926-860X(98)00170-7.

[28] Y. Iwasawa, K. Asakura, M. Tada, XAFS Techniques for Catalysts, Nanomaterials, and Surfaces, Springer International Publishing, Cham, 2017.

[29] Z. Wang, et al., Revealing brønsted acidic bridging siohal groups on amorphous silica-alumina by ultrahigh field solid-state NMR, J. Phys. Chem. Lett. 12 (47) (2021) 11563–11572, https://doi.org/10.1021/acs.jpclett.1c02975.

[30] G. Barcaro, S. Monti, L. Sementa, V. Carravetta, Modeling nucleation and growth of ZnO nanoparticles in a low temperature plasma by reactive dynamics, J. Chem. Theory Comput. 15 (3) (2019) 2010–2021, https://doi.org/10.1021/acs.jctc.8b01222.

[31] F. Bossola, N. Scotti, F. Somodi, M. Coduri, C. Evangelisti, V. Dal Santo, Electron-poor copper nanoparticles over amorphous zirconia-silica as all-in-one catalytic sites for the methanol steam reforming, Appl. Catal. B Environ. 258 (2019), https://doi.org/10.1016/j.apcatb.2019.118016.

[32] G.X. Yan, A. Wang, I.E. Wachs, J. Baltrusaitis, Critical review on the active site structure of sulfated zirconia catalysts and prospects in fuel production, Appl. Catal. A Gen. 572 (2019) 210–225, https://doi.org/10.1016/j.apcata.2018.12.012.
[33] A. Zimina, et al., CAT-ACT - A new highly versatile x-ray spectroscopy beamline for catalysis and radionuclide science at the KIT synchrotron light facility ANKA, Rev. Sci. Instrum. 88 (11) (2017), https://doi.org/10.1063/1.4999928.
[34] B. Ravel, M. Newville, ATHENA, ARTEMIS, HEPHAESTUS: Data analysis for X-ray absorption spectroscopy using IFEFFIT, J. Synchrotron Radiat. 12 (4) (2005) 537–541, https://doi.org/10.1107/S0909049505012719.
[35] C.A. Emeis, Determination of integrated molar extinction coefficients for infrared absorption bands of pyridine adsorbed on solid acid catalysts, J. Catal. 141 (2) (1993) 347–354, https://doi.org/10.1006/jcat.1993.1145.
[36] T. Barzetti, E. Selli, D. Moscotti, L. Forni, Pyridine and ammonia as probes for FTIR analysis of solid acid catalysts, J. Chem. Soc. - Faraday Trans. 92 (8) (1996) 1401–1407, https://doi.org/10.1039/ft9969201401.
[37] B.-J. van Rossum, H. Föester, H.J.M. de Groot, High-field and high-speed CP-MAS ^{13}C NMR heteronuclear dipolar- correlation spectroscopy of solids with frequency-switched Lee–Goldburg Homonuclear decoupling, J. Magn. Reson. 519 (124) (1997) 516–519, https://doi.org/10.1006/jmre.1996.1089.
[38] B.V. Merinov, J.E. Mueller, A.C.T. Van Duin, Q. An, W.A. Goddard, ReaxFF reactive force-field modeling of the triple-phase boundary in a solid oxide fuel cell, J. Phys. Chem. Lett. 5 (22) (2014) 4039–4043, https://doi.org/10.1021/jz501891y.
[39] A.P. Thompson, et al., LAMMPS - a flexible simulation tool for particle-based materials modeling at the atomic, meso, and continuum scales, Comput. Phys. Commun. 271 (2022) 108171, https://doi.org/10.1016/j.cpc.2021.108171.
[40] L. Sarkisov, R. Bueno-Perez, M. Sutharson, D. Fairen-Jimenez, Materials informatics with PoreBlazer v4.0 and the CSD MOF database, Chem. Mater. 32 (23) (2020) 9849–9867, https://doi.org/10.1021/acs.chemmater.0c03575.
[41] P. Giannozzi, et al., QUANTUM ESPRESSO: A modular and open-source software project for quantum simulations of materials, J. Phys. Condens. Matter 21 (39) (2009), https://doi.org/10.1088/0953-8984/21/39/395502.
[42] J.P. Perdew, K. Burke, M. Ernzerhof, Generalized gradient approximation made simple, Phys. Rev. Lett. 77 (18) (1996) 3865–3868, https://doi.org/10.1103/PhysRevLett.77.3865.
[43] S. Grimme, Semiempirical GGA-type density functional constructed with a long-range dispersion correction, J. Comput. Chem. 32 (2012) 174–182, https://doi.org/10.1002/jcc.20495.
[44] C.J. Pickard, F. Mauri, All-electron magnetic response with pseudopotentials: NMR chemical shifts, Phys. Rev. B Condens. Matter Mater. Phys. 63 (24) (2001) 2451011–2451013, https://doi.org/10.1103/physrevb.63.245101.
[45] F. Farges, The structure of metamict zircon: a temperature-dependent EXAFS study, Phys. Chem. Miner. 20 (7) (1994) 504–514, https://doi.org/10.1007/BF00203221.
[46] S. Foraita, et al., Impact of the oxygen defects and the hydrogen concentration on the surface of tetragonal and monoclinic ZrO2 on the reduction rates of stearic acid on Ni/ZrO2, Chem. Eur. J. 21 (6) (2015) 2423–2434, https://doi.org/10.1002/chem.201405312.
[47] G. Mountjoy, et al., Changes in the Zr environment in zirconia–silica xerogels with composition and heat treatment as revealed by Zr K-edge XANES and EXAFS, Phys. Chem. Chem. Phys. 2 (10) (2000) 2455–2460, https://doi.org/10.1039/a910300g.
[48] J.H. Choy, J.B. Yoon, H. Jung, J.H. Park, Zr K-edge XAS and 29Si MAS NMR studies on hexagonal mesoporous zirconium silicate, J. Porous Mater. 11 (3) (2004) 123–129, https://doi.org/10.1023/B:JOPO.0000038007.82949.e1.
[49] T. Lopez, J. Navarrete, R. Gomez, O. Novaro, F. Figueras, and H. Armendariz, Preparation of sol-gel sulfated ZrO23SiO2 and characterization of its surface acidity, Appl. Catal. A, Gen., 125(2), 217–232, 1995, doi: 10.1016/0926-860X(95)00022-4.
[50] Y. Zhang, L. Pan, C. Gao, Y. Wang, Y. Zhao, Preparation of ZrO2-SiO2 mixed oxide by combination of sol-gel and alcohol-aqueous heating method and its application in tetrahydrofuran polymerization, J. Sol. Gel Sci. Technol. 56 (1) (2010) 27–32, https://doi.org/10.1007/s10971-010-2268-8.
[51] M. Andrianainarivelo, R. Corriou, D. Leclercq, P.H. Mutin, A. Vioux, Mixed oxides SiO2-ZrO2 and SiO2-TiO2 by a non-hydrolytic sol-gel route, J. Mater. Chem. 6 (10) (1996) 1665–1671, https://doi.org/10.1039/JM9960601665.
[52] A. Jystad, M. Caricato, Computational multinuclear NMR characterization of metal-doped amorphous silica catalysts, Chem. Mater. 30 (21) (2018) 7813–7822, https://doi.org/10.1021/acs.chemmater.8b03257.
[53] O.B. Lapina, D.F. Khabibulin, V.V. Terskikh, Multinuclear NMR study of silica fiberglass modified with zirconia, Solid State Nucl. Magn. Reson. 39 (3–4) (2011) 47–57, https://doi.org/10.1016/j.ssnmr.2010.12.002.
[54] S.A. Sheikholeslam, J. López-Zorrilla, H. Manzano, S. Pourtavakoli, A. Ivanov, Relationship between atomic structure, composition, and dielectric constant in Zr-SiO2glasses, ACS Omega 6 (43) (2021) 28561–28568, https://doi.org/10.1021/acsomega.1c02533.
[55] V.M. Mastikhin, et al., High-resolution solid-state NMR studies of sulfate-promoted zirconia in relation to n-pentane isomerization, J. Mol. Catal. A. Chem. 101 (1) (1995) 81–90, https://doi.org/10.1016/1381-1169(95)00080-1.
[56] J.M. Miller, L.J. Lakshmi, Spectroscopic characterization of sol-gel-derived mixed oxides, J. Phys. Chem. B 102 (34) (1998) 6465–6470, https://doi.org/10.1021/jp9810771.
[57] A.A. Gabrienko, I.G. Danilova, S.S. Arzumanov, L.V. Pirutko, D. Freude, A. G. Stepanov, Direct measurement of zeolite Brønsted acidity by FTIR spectroscopy: solid-state 1H MAS NMR approach for reliable determination of the integrated molar absorption coefficients, J. Phys. Chem. C 122 (44) (2018) 25386–25395, https://doi.org/10.1021/acs.jpcc.8b07429.
[58] J. Huang, Y. Jiang, V.R. Reddy Marthala, Y.S. Ooi, J. Weitkamp, M. HungerConcentration and acid strength of hydroxyl groups in zeolites La,Na-X and La,Na-Y with different lanthanum exchange degrees studied by solid-state NMR spectroscopy, Microporous Mesoporous Mater., 104, no. 1–3, pp. 129–136, 2007, doi: 10.1016/j.micromeso.2007.01.016..
[59] Z. Zhao, et al., Structural investigation of interlayer-expanded zeolite by hyperpolarized 129Xe and ^{1}H NMR spectroscopy, Microporous Mesoporous Mater. 288 (2019) 109555, https://doi.org/10.1016/j.micromeso.2019.06.017.
[60] A. Zheng, H. Zhang, L. Chen, Y. Yue, C. Ye, F. Deng, Relationship between 1H chemical shifts of deuterated pyridinium ions and brønsted acid strength of solid acids, J. Phys. Chem. B 111 (12) (2007) 3085–3089, https://doi.org/10.1021/jp067340c.
[61] Y. Jiang, J. Huang, W. Dai, M. Hunger, Solid-state nuclear magnetic resonance investigations of the nature, property, and activity of acid sites on solid catalysts, Solid State Nucl. Magn. Reson. 39 (3–4) (2011) 116–141, https://doi.org/10.1016/j.ssnmr.2011.03.007.
[62] I.D. Gay, The 13C chemical shifts of pyridinium ion in the adsorbed state, J. Catal. 432 (1077) (1977) 430–432, https://doi.org/10.1016/0021-9517(77)90120-8.
[63] Y. eun Kim, et al., Effect of Ba impregnation on Al2O3 catalyst for 1-octene production by 1-octanol dehydration, Fuel 281 (2020) 118791, https://doi.org/10.1016/j.fuel.2020.118791.
[64] M. He, M. Wang, G. Tang, Y. Fang, T. Tan, From medium chain fatty alcohol to jet fuel: rational integration of selective dehydration and hydro-processing, Appl. Catal. A Gen. 550 (2018) 160–167, https://doi.org/10.1016/j.apcata.2017.11.009.
[65] N.M. Bertero, A.F. Trasarti, C.R. Apesteguía, A.J. Marchi, Liquid-phase dehydration of 1-phenylethanol on solid acids: influence of catalyst acidity and pore structure, Appl. Catal. A Gen. 458 (2013) 28–38, https://doi.org/10.1016/j.apcata.2013.03.018.
[66] C.P. Nash, et al., Mixed alcohol dehydration over Brønsted and Lewis acidic catalysts, Appl. Catal. A Gen. 510 (2016) 110–124, https://doi.org/10.1016/j.apcata.2015.11.019.